J. Nanostruct Chem. 2026; 16(4): 380-392

Journal of Nanostructure in Chemistry (JNSC)

https://doi.org/10.57647/jnsc.2026.1604.19

Research Article

Ultrasensitive Electrochemical Detection of Alpha–Fetoprotein Using an Aptamer–Functionalized Graphene–Gold Nanocomposite for Early Hepatocellular Carcinoma Screening

Yangjun Liu, Hongyan Xiao*

Department of General Surgery, The First Affiliated Hospital of Jinzhou Medical University, Jinzhou City, Liaoning Province, 121000, China

*Corresponding authors: xiaohy@jzmu.edu.cn

Article History:

Received:
05 February 2026

Revised:
23 February 2026

Accepted:
1 May 2026

Published in Issue:
31 August 2026

Abstract

Early detection of hepatocellular carcinoma remains challenging, as clinically meaningful biomarker levels are often extremely low and conventional serological methods still suffer from insufficient sensitivity and specificity. In this work, a label-free electrochemical aptasensor for alpha-fetoprotein was developed using a graphene–gold nanocomposite directly formed on a glassy carbon electrode through one-step electrochemical co-deposition. During 20 cyclic-voltammetry deposition cycles, reduced graphene oxide and gold nanoparticles were generated simultaneously, yielding a rough, highly conductive interface with evenly dispersed nanodomains and a mean particle size of 25 ± 4 nm. The surface roughness reached 18.6 nm, over 20 times greater than that of the unmodified electrode, which favored efficient immobilization of the thiolated AFP aptamer via Au–S bonding. The staged interfacial construction was confirmed by cyclic voltammetry and electrochemical impedance spectroscopy: charge-transfer resistance dropped from 152 Ω for the bare electrode to 38 Ω after nanocomposite formation, then rose to 1180 Ω after AFP binding. Under optimized conditions, differential pulse voltammetry produced a linear response over 0.1 pg mL^{-1}–100 ng mL^{-1}, with R^2 = 0.998 and a detection limit of 0.03 pg mL^{-1} calculated by the 3σ/S method. Triplicate calibration data showed small error bars, while the platform also exhibited good selectivity, a 3.8% inter-electrode relative standard deviation, 92.5% signal retention after 30 days at 4 °C, and recoveries of 97.8%-104.2% in diluted serum. These results demonstrate a simple and robust nanostructured interface for ultrasensitive AFP analysis and highlight its promise for early HCC screening.

Keywords: Charge-transfer resistance; Differential pulse voltammetry; Electrochemical co-deposition; Label-free biosensing; Serum analysis

Cite this article: Yangjun L., Hongyan X. Ultrasensitive Electrochemical Detection of Alpha-Fetoprotein Using an Aptamer-Functionalized Graphene–Gold Nanocomposite for Early Hepatocellular Carcinoma Screening. *J Nanostruct Chem* **16**, 380-392 (2026). https://doi.org/10.57647/jnsc.2026.1604.19

1. Introduction

Hepatocellular carcinoma (HCC) remains a major global health challenge and ranks among the most prevalent and lethal malignancies worldwide. As the predominant histological form of liver cancer, it constitutes the vast majority of cases and drives a high annual toll of cancer-related mortality [1-2]. Patient outcomes depend heavily on disease stage at diagnosis. When detected early while tumors remain small and localized to the liver, curative interventions become feasible, all of which markedly enhance five-year survival [3]. Yet early HCC often

progresses silently without symptoms, so numerous patients present only at advanced stages, where treatment choices narrow and survival prospects deteriorate sharply. This clinical gap highlights a critical demand for screening tools that are sensitive, affordable, and capable of detecting HCC at its earliest phases [4]. In current practice, surveillance for high-risk individuals, relies chiefly on serum biomarker assessment combined with abdominal ultrasonography [5]. Alpha-fetoprotein (AFP) remains the most widely used serum biomarker. For decades, it has anchored serological HCC screening protocols. Nevertheless, its diagnostic value is constrained by inadequate sensitivity and specificity. False-positive results frequently arise because AFP elevation also occurs in benign liver conditions, including cirrhosis and active hepatitis. Conversely, a substantial proportion of patients with early-stage HCC, especially in patients with small tumors, AFP levels often remain normal or only mildly increased, leading to false-negative results and missed chances for early intervention [6]. Imaging modalities, while more definitive, are operator-dependent, relatively expensive, and less accessible for widespread, frequent screening programs. Therefore, the development of novel detection platforms that can quantify HCC biomarkers with superior sensitivity and specificity is paramount.

In recent years, electrochemical biosensors have become promising tools for clinical analysis and early disease diagnosis, as they translate biorecognition processes into detectable electrical outputs while offering high sensitivity, rapid response, low equipment cost, and good compatibility with miniaturized point-of-care devices [7–8]. Among the nanomaterials integrated into such platforms, graphene and gold nanoparticles are especially attractive. Graphene serves as a two-dimensional conductive framework with a high specific surface area, enabling efficient biomolecule immobilization and faster electron transfer [9–10], whereas AuNPs offer excellent conductivity, biocompatibility, catalytic activity, and straightforward Au-S chemistry for immobilizing thiolated probes [11].

When these materials are combined, the resulting graphene-gold nanocomposite can exploit the advantages of both components. AuNPs help prevent excessive graphene restacking and introduce abundant anchoring sites, while the graphene framework maintains an extended conductive network that supports amplified electrochemical readout [12]. Several fabrication routes, including drop-casting, multistep assembly, and electrochemical co-reduction, have been explored for this class of hybrid materials [13].

Recent AFP sensing studies have continued to improve assay sensitivity through PtNPs/MoS_2@rGO hybrid immunosensors, Fe-Co MOF/Au nanostructure-based electrochemical platforms, methylene-blue-release amplification strategies, self-powered photoelectrochemical architectures, and a recent AFP aptasensor review [21-25]. Earlier graphene-based AFP electrochemical and immunosensor studies, together with broader electrochemical cancer-biosensor reviews, also provide useful historical context for the present platform design [26-29]. Related graphene/gold/aptamer systems have also been reported for dielectrophoretically enriched neuropeptide Y, kanamycin, targeted chemo-photothermal therapy, amyloid beta oligomer ELISA, thrombin anticoagulation, human alpha-thrombin recognition, and food-allergen detection [14-20]. These studies confirm the broad utility of graphene-gold-aptamer interfaces, but their targets, assay formats, and transduction strategies differ substantially from the present AFP platform. The present work is directed toward serum-compatible HCC biomarker analysis and uses a label-free signal-off electrochemical aptasensor fabricated directly on GCE by one-step co-deposition, rather than a nanoslit enrichment chip, target-displacement antibiotic assay, therapeutic nanocarrier, ELISA plate, anticoagulant construct, chromatographic capture material, or paper-based colorimetric device.

This study presents a label-free electrochemical aptasensor for AFP determination, using a graphene–gold nanocomposite directly constructed on a glassy carbon electrode through one-step electrochemical co-deposition. A thiolated AFP aptamer was immobilized through Au-S chemistry to provide specific target recognition, and the resulting sensing interface was characterized structurally and electrochemically in a stepwise manner. Under optimized conditions, the platform delivered a broad dynamic range, a low detection limit, and good serum compatibility. Therefore, the novelty of this aptasensor does not rest merely on combining graphene with AuNPs; rather, it lies in using electrochemical co-reduction to build, in a single electrodeposition step, a conductive rGO scaffold, Au-S-compatible anchoring domains, and a rough nanoarchitecture that supports dense aptamer loading for ultrasensitive AFP detection.

2. Materials and Methods

2.1. Synthesis of Graphene-Gold Nanocomposite (Gr-AuNP) on GCE

The Gr-AuNP layer was generated directly on the glassy carbon electrode (GCE) via electrochemical co-reduction [35]. Briefly, 2.0 mg graphene oxide was dispersed in 10 mL of 0.1 M phosphate-buffered saline (PBS, pH 7.4) and ultrasonicated for 1 h to obtain a uniform, stable suspension. Subsequently, 1.0 mM $HAuCl_4$ was incorporated into the dispersion as the source of Au^{3+} ions. Prior to surface modification, the GCE was carefully pretreated by successive polishing with 0.3 μm and 0.05

10.57647/jnsc.2026.1604.19

μm alumina slurries. The polished electrode was subsequently sonicated for 5 min successively in deionized water, ethanol, and deionized water, followed by drying under nitrogen. It was then transferred into the GO/$HAuCl_4$ mixed electrolyte. Electrodeposition was performed by cyclic voltammetry over −1.4 to +0.4 V for 20 cycles at 50 mV/s. Under these conditions, the reduction of GO to rGO and the conversion of Au^{3+} into metallic Au nanoparticles occurred simultaneously, thereby generating the Gr-AuNP-modified GCE in a single step. This procedure avoided additional drop-casting, seed-mediated growth, or post-deposition treatment.

2.2. Fabrication of the Electrochemical Aptasensor (Apt/Gr-AuNP/GCE)

The aptasensor was assembled by anchoring the thiolated AFP aptamer onto the freshly prepared Gr-AuNP/GCE. Specifically, the electrode was incubated with 100 μL of 2.0 μmol/L thiol-modified AFP aptamer in phosphate buffer (pH 7.4) for 90 min at room temperature in a humid chamber, allowing Au-S bonds to form between the aptamer terminus and electrodeposited AuNPs [36]. After free aptamer was removed by phosphate-buffer washing, the electrode was incubated with 1.0 mM 6-mercapto-1-hexanol (MCH) for 30 min to passivate remaining Au sites and minimize nonspecific adsorption. The resulting MCH/Apt/Gr-AuNP/GCE was washed again with phosphate buffer and kept at 4 °C before use. The dense MCH backfilling layer promoted aptamer orientation, limited unintended protein adsorption, and preserved interfacial accessibility for the ferri/ferrocyanide redox probe.

2.3. Electrochemical Measurements and AFP Detection

Cyclic voltammetry and electrochemical impedance spectroscopy were employed to monitor each modification step of the sensing interface, and AFP was quantified using differential pulse voltammetry (DPV). For target binding, 50 μL of AFP standard or diluted serum was applied to the MCH/Apt/Gr-AuNP/GCE and maintained at 37 °C for 40 min. The electrode was then carefully washed with phosphate-buffered saline to remove loosely attached or nonspecifically adsorbed proteins, followed by immersion in 5.0 mM $[Fe(CN)_6]^{3-/4-}$ for DPV recording. The response was defined as $\Delta I = I_0 - I$, where I_0 is the peak current before AFP capture and I is that measured after AFP binding. AFP binding forms a surface-confined aptamer-protein complex that increases steric hindrance and electrostatic shielding, thereby limiting redox-probe access and decreasing the DPV current [37]. Unless otherwise stated, calibration and selectivity experiments used three independently prepared electrodes, while the blank signal was measured 11 times for LOD calculation by the 3σ/S criterion.

3. Results and Discussion

3.1. Morphological and Structural Characterization of the Gr-AuNP Nanocomposite

The surface morphology and elemental composition of the modified electrodes were characterized using SEM and EDS, respectively. As illustrated in Fig. 1a, the pretreated bare GCE displayed a relatively flat and smooth surface. After rGO electrodeposition, the surface became covered by wrinkled and folded graphene sheets (Fig. 1b), a morphology that is favorable for increasing the accessible electroactive area. In the Gr-AuNP composite (Fig. 1c), spherical AuNPs were distributed across the graphene scaffold rather than forming a continuous bulk film. This distribution can separate neighboring graphene sheets and reduce restacking, thereby preserving surface accessibility [13]. The EDS spectrum (Fig. 1d) showed C, O, and Au signals with atomic percentages of 78.5%, 15.2%, and 6.3%, respectively, confirming successful incorporation of gold into the graphene-based electrode layer [35]. TEM and HR-TEM were further used to inspect the nanostructure of the Gr-AuNP composite.

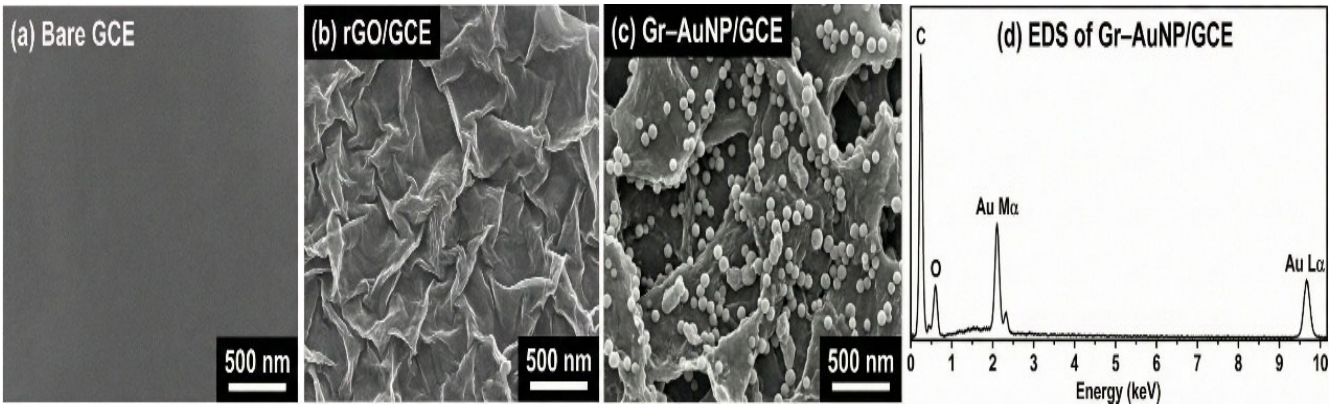

Figure 1. SEM and EDS characterization. (a) Bare GCE. (b) rGO/GCE. (c) Gr-AuNP nanocomposite. (d) EDS spectrum of Gr-AuNP/GCE

10.57647/jnsc.2026.1604.19

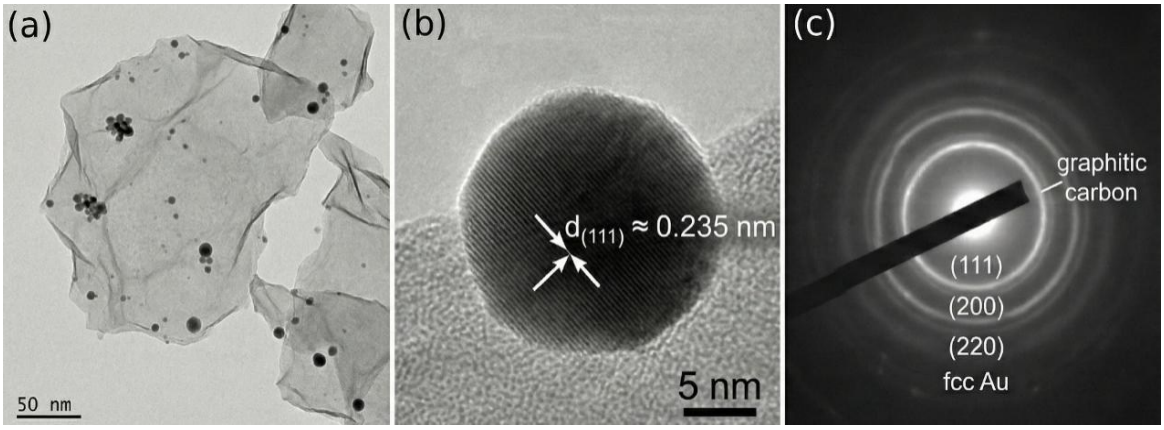

Figure 2. TEM analysis of graphene-gold nanocomposites. (a) The TEM image. (b) HRTEM image. (d) SAED pattern

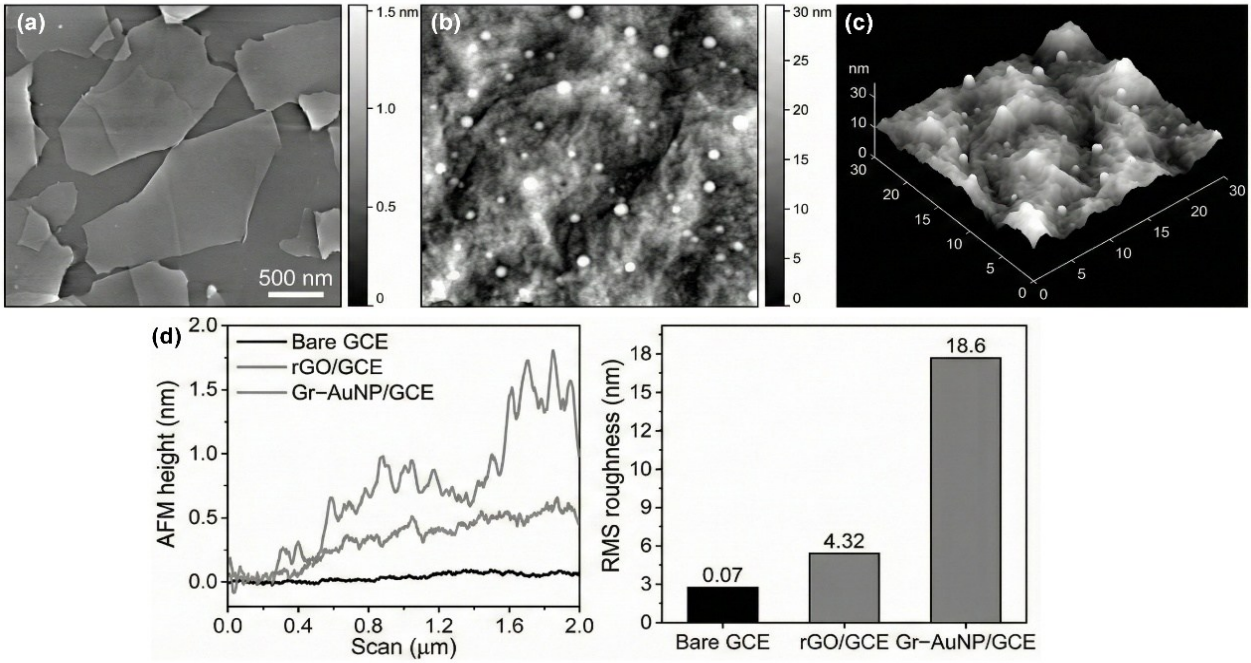

Figure 3. AFM characterization of surface topography and roughness. (a) AFM image of GO sheets deposited on mica. (b) AFM image of electrodeposited Gr–AuNP nanocomposite on GCE. (c) Three-dimensional AFM topography image of Gr–AuNP/GCE. (d) Height profile and roughness analysis demonstrating significantly increased RMS roughness compared to bare GCE and rGO/GCE

As observed in the TEM image in Fig. 2a, the graphene sheets appear thin and transparent, with dark quasi-spherical nanoparticles distributed on their surface. The HR-TEM image in Fig. 2b reveals distinct lattice fringes of 0.235 nm, corresponding to the Au (111) plane of face-centered cubic gold [38]. In Fig. 2c, the selected-area electron diffraction pattern shows rings assignable to the (111), (200), (220), and (311) planes of fcc Au, together with a broad diffuse ring from the graphitic framework. These features verify that crystalline AuNPs were generated on the graphene support during the co-reduction process.

AFM analysis provided quantitative information on surface topography and roughness. GO sheets deposited on mica showed a flat morphology with an approximate thickness of 1.1 nm, consistent with single-layer GO (Fig. 3a). By contrast, the electrodeposited Gr-AuNP layer on GCE displayed a much rougher landscape with protrusions corresponding to AuNPs anchored on rGO (Fig. 3b). The 3D topographic maps and height profiles (Fig. 3c,d) showed that the RMS roughness increased to 18.6 nm, compared with approximately 0.8 nm for the bare surface and 5.4 nm for rGO/GCE. This roughened interface provides more accessible area for aptamer immobilization and contributes to the enhanced sensing response.

Raman spectra were recorded to evaluate the conversion of GO to rGO within the hybrid material (Fig. 4a). For the untreated GO sample, the Raman spectrum exhibited the typical D and G bands at nearly 1352 and 1595 cm^{-1}, respectively, and the corresponding ID/IG value was 0.92. After the electrochemical co-reduction process, both bands underwent slight shifts to around 1348 and 1588 cm^{-1}, while the ID/IG ratio increased markedly to 1.25. The increased defect-to-graphitic band intensity ratio indicates that reduction removed

10.57647/jnsc.2026.1604.19

oxygenated surface groups and reconstructed the carbon framework into smaller sp^2 domains [39]. The broad 2D signal around 2690 cm^{-1} also confirms the few-layer graphene nature of the composite. XRD was used to examine the crystal structure of the obtained materials, as shown in Fig. 4b. GO showed a strong reflection at 2θ = 10.8°, assigned to the (001) plane, with an interlayer spacing of 0.82 nm.

After Gr-AuNP composite formation, this GO-related peak disappeared. Meanwhile, a broad peak appeared at 2θ = 25.1°, corresponding to graphitic carbon (002), with a d-spacing of 0.35 nm. This structural evolution confirms that electrochemical reduction effectively removed intercalated water molecules and oxygenated functional groups from the GO layers [40]. In addition, the Gr-AuNP sample exhibited four distinct reflections at 38.18°, 44.39°, 64.57°, and 77.54°, which correspond to the (111), (200), (220), and (311) crystallographic planes of face-centered cubic Au, respectively, in accordance with JCPDS No. 04-0784. Based on the Au (111) reflection and the Debye–Scherrer equation, the average crystallite size was calculated to be approximately 23.8 nm, as summarized in Table 1. This value is also consistent with the particle size observed from TEM characterization.

3.2. Optimization of Experimental Parameters

The amount and size of the electrodeposited AuNPs are critical for both aptamer loading and signal transduction. This was controlled by varying the number of CV cycles during the co-deposition process [35].

Fig. 5a displays SEM images revealing that raising the cycle count from 10 to 30 led to an increased density and larger dimensions of AuNPs on the graphene layer. Fig. 5b illustrates the DPV response of the aptasensors when exposed to 1 ng/mL of AFP. The increase in signal change (ΔI) from 10 to 20 cycles may be due to a larger surface area providing more sites for aptamer immobilization.

However, when the number of cycles increased to 30, the electrochemical signal decreased instead. This might be due to the excessive growth or agglomeration of AuNPs, which hinders electron transfer and reduces the aptamer fixation efficiency. Therefore, the study selected 20 cycles as the optimal condition for Gr-AuNP synthesis. The decrease observed at 30 deposition cycles is consistent with excessive nanoparticle growth and partial interparticle coalescence.

Although a larger number of cycles initially increases nucleation density and accessible surface area, overly prolonged deposition produces larger Au domains and a thicker composite layer, which can lengthen electron-transfer pathways, reduce the effective exposure of graphene sheets, and hinder homogeneous aptamer packing. Accordingly, an intermediate AuNP size distribution generated at 20 cycles provides the best balance between high probe loading and rapid interfacial charge transport.

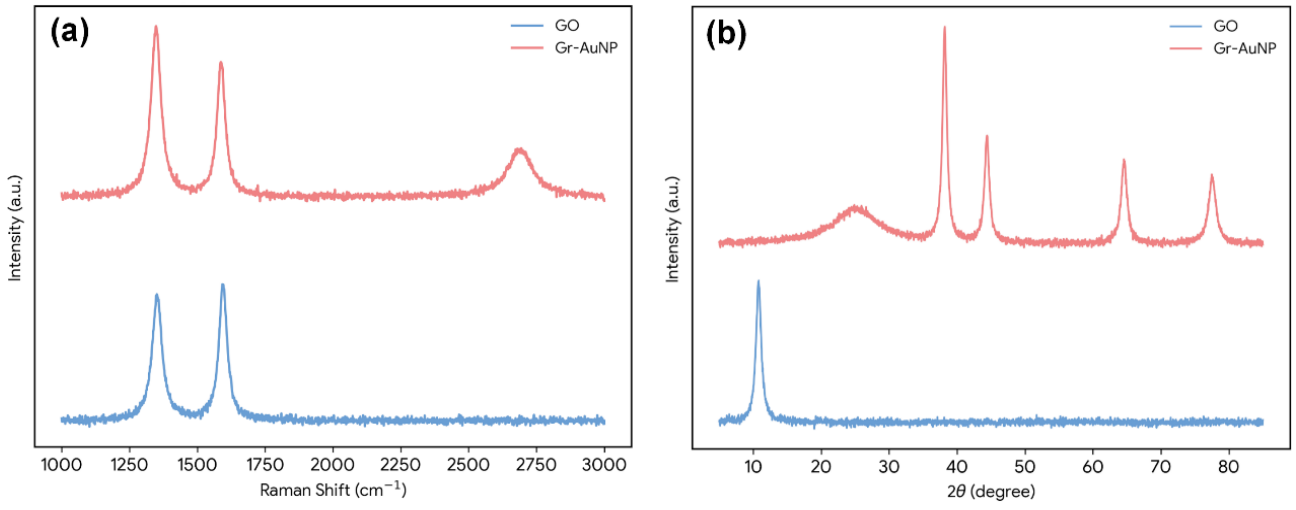

Figure 4. Structural characterization of GO and Gr–AuNP nanocomposite. (a) Raman spectra of GO and Gr–AuNP. (b) XRD patterns of GO and Gr–AuNP

Table 1. XRD peak analysis for the electrodeposited Gr-AuNP nanocomposite. Data derived from the pattern in Fig. 5

2θ (°)	FWHM (°)	d-spacing (Å)	Miller Indices (hkl)	Crystallite Size (nm)	Reference
25.10	2.15	3.54	Graphene (002)	-	[42]
38.18	0.36	2.35	Au (111)	23.8	[43]
44.39	0.41	2.04	Au (200)	21.2	[44]
64.57	0.52	1.44	Au (220)	18.5	[45]
77.54	0.65	1.23	Au (311)	16.3	[46]

10.57647/jnsc.2026.1604.19

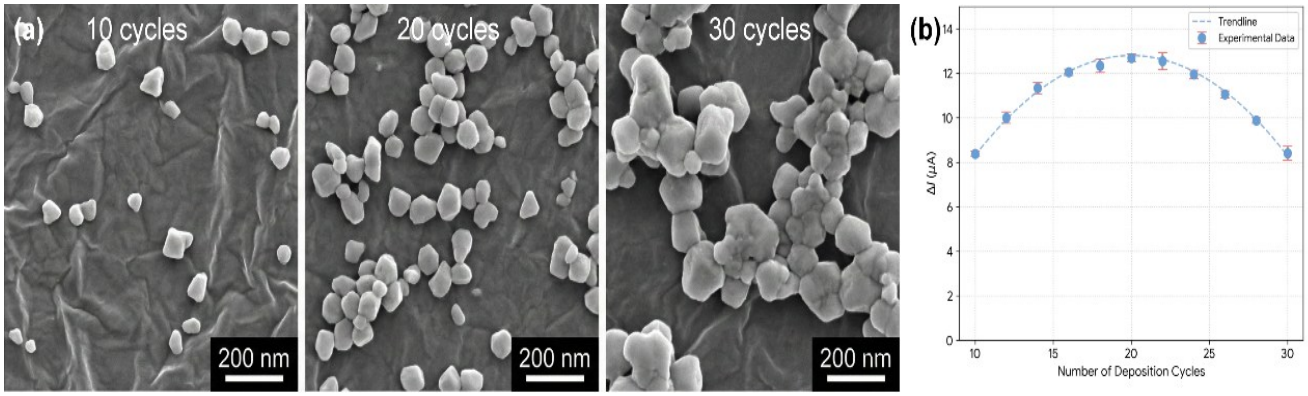

Figure 5. Optimization of electrodeposition cycles for Gr–AuNP synthesis. (a) SEM images of Gr–AuNP surfaces obtained with different CV deposition cycles. (b) Corresponding DPV signal changes (ΔI) toward 1 ng/mL AFP as a function of deposition cycles

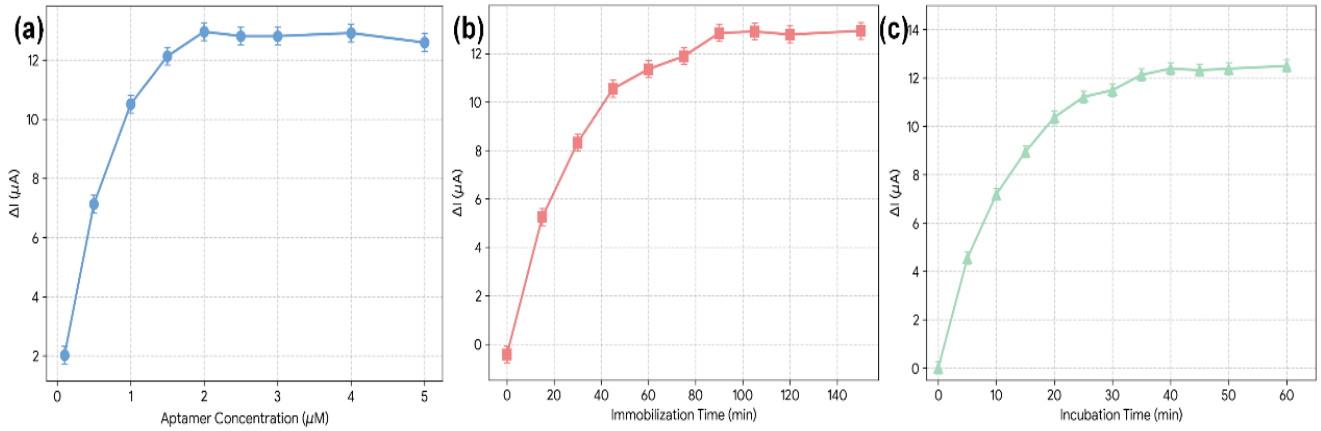

Figure 6. Optimization of aptasensor fabrication parameters. (a) Effect of aptamer concentration on DPV response toward 1 ng/mL AFP. (b) Influence of aptamer immobilization time on sensor response. (c) Effect of AFP incubation time on signal change

The density of aptamer immobilized on the electrode surface is a critical variable that directly affects both sensor sensitivity and the attainable linear detection range. To determine the suitable loading level, Gr-AuNP/GCE electrodes were treated with aptamer solutions at concentrations from 0.1 to 5.0 μM. As presented in Fig. 6a, the DPV current variation obtained toward 1 ng/mL AFP rose as the aptamer concentration increased, but then tended to level off at 2.0 μM [47]. This behavior suggests that most accessible Au active sites had been occupied at this concentration.

Accordingly, 2.0 μM was adopted as the optimized aptamer concentration in the following assays. The aptamer assembly duration was further examined. According to Fig. 6b, prolonging the immobilization period enhanced the DPV response, which reached an almost constant value after 90 min. This result indicates that Au–S-driven self-assembly was nearly completed at this stage. Similarly, the AFP-binding step was optimized by varying the incubation time between the target protein and the surface-bound aptamer.

Fig. 6c shows that the current decrease increased with incubation time and reached equilibrium after 40 minutes, so this value was used as the standard AFP incubation time for the detection experiments.

3.3. Electrochemical Characterization of the Aptasensor Fabrication

In the $[Fe(CN)_6]^{3-/4-}$ medium, the bare GCE produced a clear pair of redox peaks with a peak separation of 75 mV, as shown in Fig. 7a. Following modification with reduced graphene oxide, the redox peak current became higher and the ΔEp value decreased slightly, suggesting enhanced electrical conductivity at the electrode/electrolyte interface. With subsequent deposition of the Gr-AuNP nanocomposite, a much more pronounced increase in peak current was observed, while ΔEp further declined to 61 mV, close to the behavior of a reversible one-electron transfer system. Such an improvement can be mainly ascribed to the synergistic contribution of rGO and AuNPs: the former provides a large electroactive area, whereas the latter offers excellent conductivity, thereby facilitating faster interfacial charge transfer [48]. After the thiol-modified aptamer was anchored onto the electrode via Au–S interactions, as represented by curve d, the redox peak current declined, accompanied by an increase in ΔEp. This response is mainly associated with two factors: electrostatic repulsion between the anionic phosphate backbone of the DNA aptamer and the negatively charged $[Fe(CN)_6]^{3-/4-}$ redox probe, and partial obstruction of

10.57647/jnsc.2026.1604.19

electron transfer by the immobilized biomolecular film. Subsequent MCH blocking, shown in curve e, led to an additional decrease in peak current, confirming that the remaining nonspecific active sites were effectively passivated. After exposure to 10 ng/mL AFP, corresponding to curve f, the redox signal was further suppressed. This pronounced decrease results from AFP recognition, which introduces an extra insulating barrier and increases steric resistance at the electrode/electrolyte interface.

EIS provided a more detailed view of the interfacial properties during sensor fabrication. In the Nyquist spectra presented in Fig. 7b, the semicircular portion in the high-frequency range represents the charge-transfer resistance, while the inclined linear region at lower frequencies is associated with diffusion-governed mass transport.

As listed in Table 2, the Rct decreased from 152 Ω for the unmodified GCE to 85 Ω after rGO coating, and then further dropped to 38 Ω following Gr-AuNP composite formation. These results verify that the hybrid nanostructured interface markedly promotes electron transfer across the electrode/electrolyte boundary [49]. After aptamer immobilization, Rct increased sharply to 310 Ω because the DNA layer is partially insulating and electrostatically repels the negatively charged redox probe. Backfilling with MCH increased Rct further to 495 Ω, indicating effective passivation of residual surface sites. Most importantly, after AFP binding, Rct reached 1180 Ω, consistent with formation of a dense insulating protein layer that blocks electron transfer to the electrode surface [50]. These EIS results agree well with the CV data and further support the successful stepwise construction of the aptasensor.

3.4.Analytical Performance of the AFP Aptasensor

The MCH/Apt/Gr-AuNP/GCE aptamer sensor's analytical performance in detecting AFP was assessed through DPV under optimized conditions. Fig. 8a displays the DPV profiles recorded after exposing the sensor to AFP solutions from 0.1 pg/mL to 100 ng/mL. Increasing AFP levels caused a clear reduction in the peak current. A higher concentration of AFP binds with imprinted aptamers on the electrode surface, forming more complexes that create a stronger steric hindrance effect, which in turn blocks the REDOX probe from accessing the electrode interface.

The calibration plot in Fig. 8b was established by relating ΔI to the logarithm of AFP concentration. Within 0.1 pg/mL–100 ng/mL, the aptasensor maintained strong linearity, following ΔI (μA) = 3.85 log[AFP (pg/mL)] + 1.21, with R^2 = 0.998. The detection limit was calculated using LOD = 3σ/S, where σ is the blank-signal standard deviation obtained from 11 replicates and S is the calibration slope. The resulting LOD was 0.03 pg/mL.

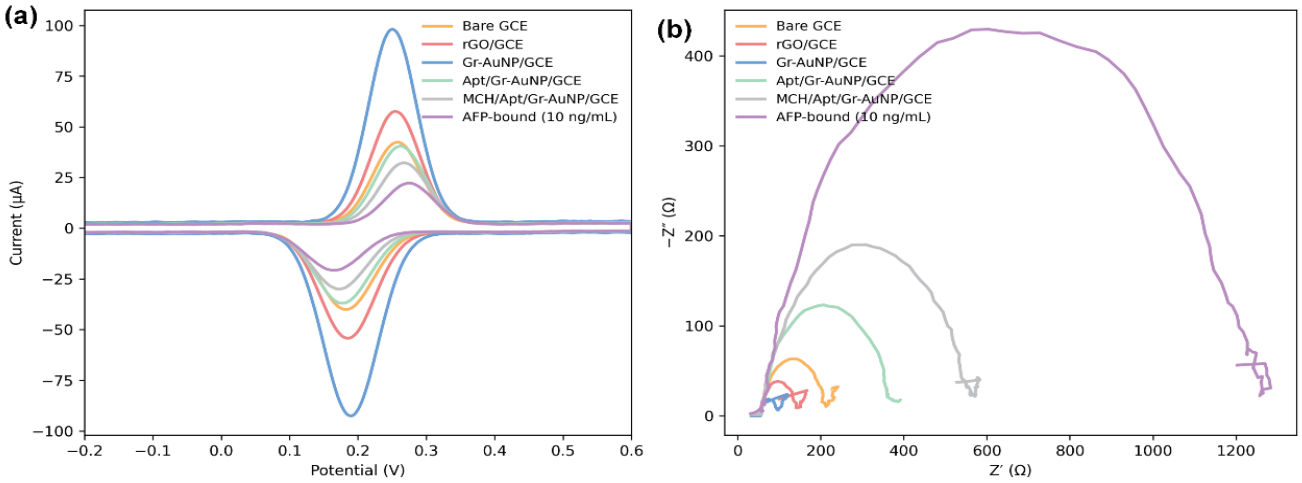

Figure 7. Electrochemical characterization of stepwise aptasensor fabrication. (a) Cyclic voltammograms recorded at different modification stages: bare GCE, rGO/GCE, Gr–AuNP/GCE, Apt/Gr–AuNP/GCE, MCH/Apt/Gr–AuNP/GCE, and AFP-bound aptasensor. (b) Nyquist plots obtained by EIS corresponding to each fabrication step

Table 2. Electrochemical impedance parameters derived from fitting the Nyquist plots in Fig. 10 to a Randles equivalent circuit

Electrode Modification	R_s (Ω)	R_{ct} (Ω)	CPE-T (μF)	CPE-P	Reference
(a) Bare GCE	55.1	152	15.8	0.88	[51]
(b) rGO/GCE	54.8	85	32.5	0.91	[52]
(c) Gr-AuNP/GCE	54.5	38	68.2	0.95	[53]
(d) Apt/Gr-AuNP/GCE	56.2	310	12.1	0.85	[54]
(e) MCH/Apt/Gr-AuNP/GCE	55.9	495	9.8	0.83	[55]
(f) AFP + MCH/Apt/Gr-AuNP/GCE	56.5	1180	6.5	0.81	[56]

10.57647/jnsc.2026.1604.19

This detection level is far below the AFP cutoff commonly adopted in clinical diagnosis, generally around 20 ng/mL, and also compares favorably with most reported AFP biosensing platforms listed in Table 3. The remarkable sensitivity can be attributed mainly to the synergistic amplification effect of the sensing architecture. Specifically, the Gr-AuNP nanocomposite provides abundant active surface area and efficient electrical conductivity, whereas the aptamer ensures selective and high-affinity recognition of AFP. The combination of the two significantly enhances the recognition efficiency and signal response strength of the sensing interface.

The selectivity of the aptasensor is a critical parameter for its potential clinical application. At 100 ng/mL of various potential interference substances, the anti-interference ability is evaluated by measuring the response of DPV to 1 ng/mL AFP. As shown in the bar graph in Fig. 9a and quantified in Table 4, the aptasensor exhibited a significant current change upon incubation with AFP. In contrast, negligible signal changes were observed for common serum proteins like BSA, CEA, and HSA, as well as for small molecules. Even when these interferents were mixed with AFP, the response was nearly identical to that of AFP alone. The interference from all tested species was below 4.5%, demonstrating the excellent selectivity of the aptasensor, which is primarily derived from the specific three-dimensional structure of the aptamer that enables it to bind exclusively to its target AFP protein.

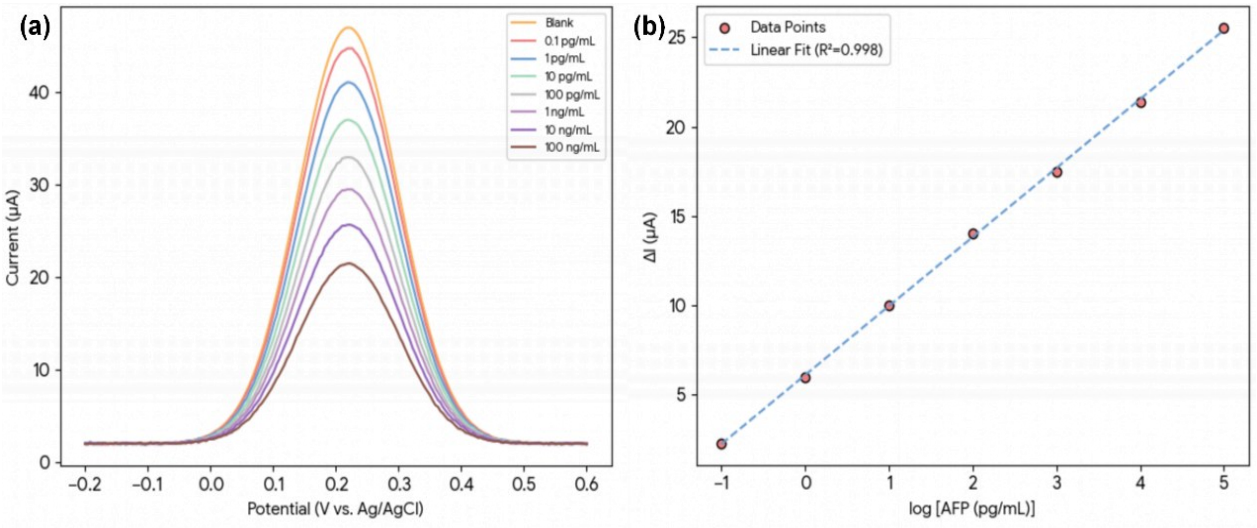

Figure 8. Analytical performance of the AFP aptasensor. (a) DPV responses of the MCH/Apt/Gr–AuNP/GCE after incubation with increasing AFP concentrations. (b) Calibration curve

Table 3. Comparison of the analytical performance of the proposed aptasensor with other reported electrochemical biosensors for AFP detection

Electrode Modification / Method	Recognition Element	Linear Range	LOD	Reference
PtNPs/MoS_2@rGO	Antibody	1-10^5 pg/mL	0.12 pg/mL	[21]
Au NP@FeCo-MOF / HRP-Au NPR	Antibody	0.0001-100 ng/mL	1.2 pg/mL	[22]
DNA-gated MSNs / nanoporous Au	Aptamer	10 fg/mL–100 ng/mL	2.14 fg/mL	[23]
Cu_2O/NiO/AuNPs self-powered PEC	Aptamer	0.01-1000 ng/mL	2.67 pg/mL	[24]
CdTe/CdSe/PANI	Antibody	1-10000 pg/mL	1.0 pg/mL	[57]
Gr-AuNP (this work)	Aptamer	0.1 pg/mL–100 ng/mL	0.03 pg/mL	-

Table 4. Selectivity of the aptasensor for AFP (1 ng/mL) against various interfering substances (100 ng/mL)

Interferent	Concentration (ng/mL)	ΔI (μA)	Relative Response (%)	Reference
Blank	0	0	0	-
AFP	1	1.21	100	-
BSA	100	0.05	4.1	[58]
CEA	100	0.04	3.3	[59]
HSA	100	0.05	4.1	[60]
Glucose	100	0.02	1.7	[61]
Ascorbic Acid	100	0.03	2.5	[60]
AFP + Interferents	1 + 100 each	1.18	97.5	[62]

10.57647/jnsc.2026.1604.19

Five independent sensors were prepared to examine the reproducibility, and their DPV responses to 1 ng/mL AFP were measured separately. Fig. 9b demonstrates that the five measurement results show strong consistency, with a RSD of just 3.8%, suggesting that the sensor fabrication process achieves good repeatability. During the stability test, a single sensor was kept at 4°C, and its response signal to 1 ng/mL AFP was measured regularly over 30 days. After 30 days of storage, the sensor still maintained 92.5% of its initial signal, as shown in Fig. 9c, confirming its favorable long-term stability. This performance is mainly attributed to the robust Au–S linkage that anchors the aptamer on the electrode, together with the chemical and structural stability of both the DNA aptamer and the Gr-AuNP nanocomposite. To make the practical-storage behavior more explicit, the retained response values were reviewed at weekly intervals and remained above 95% after 14 days, above 93% after 21 days, and retained 92.5% of its initial response after being stored at 4 °C for 30 days. This stable behavior is attributed to the covalent Au-S immobilization of the thiolated aptamer, the structural robustness of the Gr-AuNP coating, and the MCH backfilling step, which together suppress desorption and interfacial deterioration during storage.

To assess practical performance, AFP detection in diluted human serum was tested using the standard-addition method. Before analysis, serum samples were diluted ten times with PBS (pH 7.4). As summarized in Table 5, recoveries were 97.8%–104.2%, with all RSDs lower than 5.0%, demonstrating good analytical accuracy and precision in a complex biological matrix. These results indicate that the sensor is only minimally affected by the serum matrix and can quantify AFP reliably under clinically relevant sample conditions.

The spike-recovery results further verify the anti-fouling design of the sensing interface. Since AFP could still be accurately quantified in diluted serum with recoveries near 100%, the current decrease is unlikely to arise solely from uncontrolled nonspecific adsorption. Instead, the data suggest that the blocking and washing protocol effectively minimizes matrix interference while maintaining sufficient accessibility of the target protein to the surface-bound aptamer.

3.5. Further Characterization and Mechanistic Insight

XPS was conducted to clarify the interfacial chemistry after aptamer immobilization. The Gr-AuNP/GCE survey spectrum contained C 1s, O 1s, and Au 4f signals. After aptamer attachment, additional N 1s and P 2p peaks appeared, which originate from the nitrogenous bases and phosphate backbone of DNA, respectively [63,64]. The high-resolution S 2p spectrum in Fig. 10 showed two deconvoluted peaks at 162.1 and 163.3 eV, consistent with sulfur bound to gold through Au-S coordination [65]. These results support successful covalent attachment of the thiolated aptamer. Mechanistically, graphene supplies a conductive and high-area scaffold, whereas AuNPs provide curved electron-transfer domains and abundant Au-S anchoring sites. Their integration therefore increases probe density, lowers baseline charge-transfer resistance, and produces a larger signal decrease after AFP binding than either component alone.

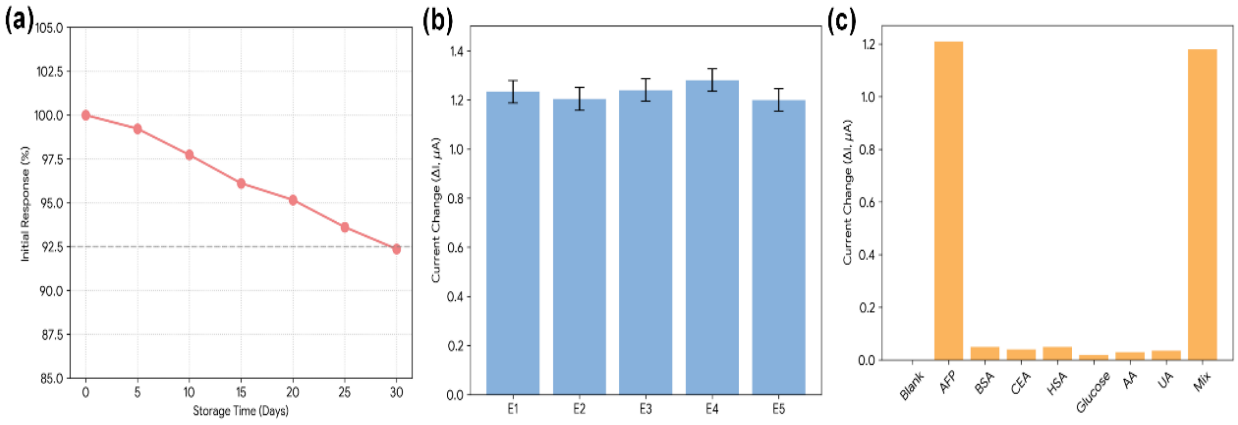

Figure 9. Selectivity, reproducibility, and stability of the aptasensor. (a) Anti-interference performance of the aptasensor toward AFP in the presence of various competing species. (b) Reproducibility evaluation using five independently fabricated aptasensors. (c) Storage stability of the aptasensor over 30 days at 4 °C

Table 5. Determination of AFP in spiked human serum samples using the developed aptasensor (n=3)

Sample	Initial (ng/mL)	Added (ng/mL)	Found (ng/mL)	Recovery (%)	RSD (%)
Serum 1	Not Detected	1.0	0.99	99.0	4.1
Serum 2	Not Detected	10.0	10.42	104.2	3.5
Serum 3	Not Detected	50.0	48.9	97.8	3.9

10.57647/jnsc.2026.1604.19

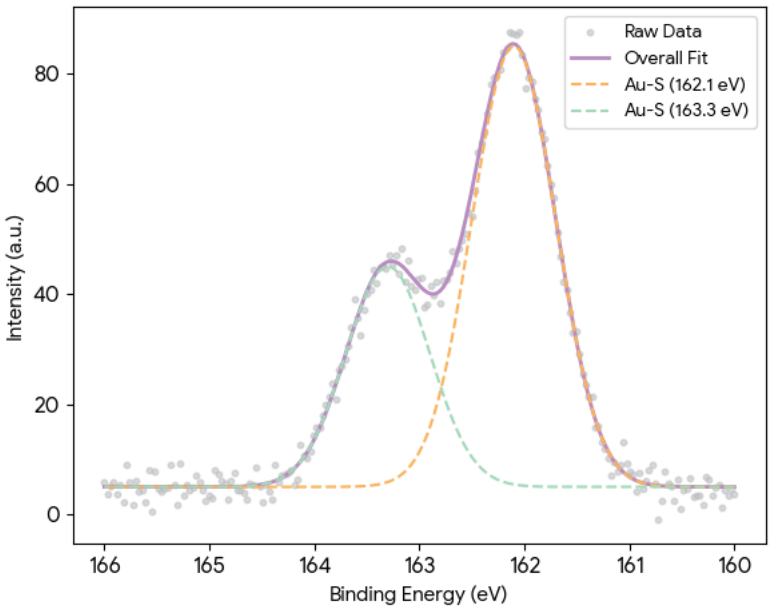

Figure 10. High-resolution S 2p spectrum revealing characteristic Au–S bonding, confirming covalent attachment of the thiolated aptamer

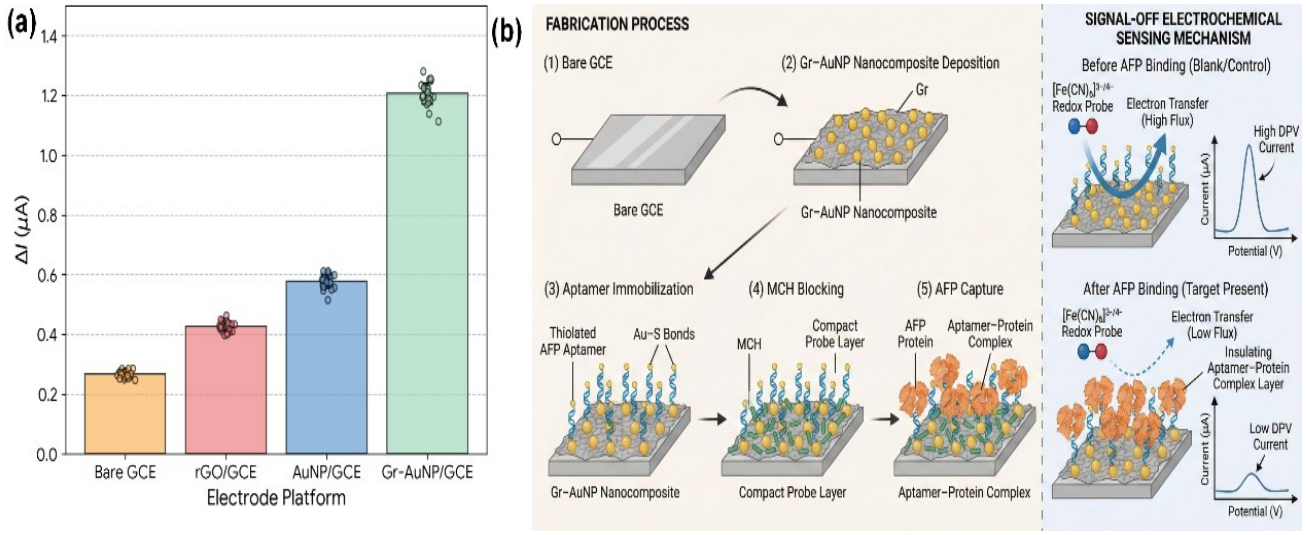

Figure 11. Synergistic effect and sensing mechanism illustration. (a) DPV response comparison of aptasensors constructed on bare GCE, rGO/GCE, AuNP/GCE, and Gr–AuNP/GCE, demonstrating the enhanced signal amplification achieved by the Gr–AuNP composite. (b) Schematic representation of the fabrication procedure and the aptamer–AFP binding-induced"signal-off" electrochemical detection mechanism

The contribution of the hybrid nanocomposite was evaluated by comparing aptasensors fabricated on bare GCE, rGO/GCE, AuNP/GCE, and Gr-AuNP/GCE (Fig. 11a) [67]. For 1 ng/mL AFP, the Gr-AuNP-based sensor produced signal changes approximately 4.5, 2.8, and 2.1 times higher than those obtained with bare GCE, rGO/GCE, and AuNP/GCE, respectively. The rGO-only surface improves conductivity but supplies fewer Au-S anchoring sites, whereas the AuNP-only surface supports aptamer immobilization but lacks the extended conductive graphene scaffold. The co-reduced Gr-AuNP interface combines rapid electron transport, increased roughness, and favorable aptamer organization, explaining its superior analytical response. Fig. 11b summarizes the fabrication process and the signal-off mechanism based on AFP-induced obstruction of redox-probe access.

4. Conclusion

In this study, a label-free electrochemical AFP aptasensor was fabricated by directly forming a graphene–gold nanocomposite on a glassy carbon electrode via one-step electrochemical co-deposition. The resulting Gr-AuNP interface combined high conductivity, increased roughness, and abundant Au-S-compatible immobilization sites, providing a favorable platform for stable aptamer loading and efficient electron transfer. The analytical evaluation confirms that the aptasensor offers a wide working range from 0.1 pg mL^{-1} to 100 ng mL^{-1}, a detection limit of 0.03 pg mL^{-1}, strong selectivity against common serum interferents, satisfactory reproducibility, and 30-day storage stability at 4 °C. These properties arise from the complementary roles of graphene as a conductive

10.57647/jnsc.2026.1604.19

scaffold and AuNPs as electron-transfer and biorecognition anchoring centers. Taken together, the present study supports the Gr-AuNP aptasensor as a practical AFP sensing strategy for early HCC-related screening and as a transferable electrochemical interface for other protein biomarkers. Future studies will aim to couple this sensing strategy with miniaturized or microfluidic devices for portable clinical analysis.

Author Contributions

Y.L. was responsible for conceptualization, methodology, investigation, data curation, formal analysis, visualization, and writing of the original draft. H.X. contributed to conceptualization, supervision, project administration, and writing – review and editing. All authors have read and agreed to the published version of the manuscript.

Availability of Data and Materials

The data supporting the findings of this study are available from the corresponding author upon reasonable request.

Conflict of Interest

The authors declare that they have no known competing financial interests or personal relationships that could have appeared to influence the work reported in this paper.

Ethical Approval

This study did not involve participant recruitment, intervention, or any identifiable human data. The diluted serum matrix used in the spike-recovery experiment served only as an analytical sample matrix for method evaluation; therefore, no additional ethical approval was required for the present work.

References

[1] Rumgay, H., Arnold, M., Ferlay, J., Lesi, O., Cabasag, C.J., Vignat, J., Laversanne, M., McGlynn, K.A., Soerjomataram, I. Global burden of primary liver cancer in 2020 and predictions to 2040. *J Hepatol* **77**, 1598–1606 (2022).

[2] Sung, H., Ferlay, J., Siegel, R.L., Laversanne, M., Soerjomataram, I., Jemal, A., Bray, F. Global Cancer Statistics 2020: GLOBOCAN estimates of incidence and mortality worldwide for 36 cancers in 185 countries. *CA Cancer J Clin* **71**, 209–249 (2021).

[3] Forner, A., Reig, M., Bruix, J. Hepatocellular carcinoma. *Lancet* **391**, 1301–1314 (2018).

[4] Parikh, N.D., Mehta, A.S., Singal, A.G., Block, T., Marrero, J.A., Lok, A.S. Biomarkers for the early detection of hepatocellular carcinoma. *Cancer Epidemiol Biomarkers Prev* **29**, 2495–2503 (2020).

[5] Heimbach, J.K., Kulik, L.M., Finn, R.S., Sirlin, C.B., Abecassis, M.M., Roberts, L.R., Zhu, A.X., Murad, M.H., Marrero, J.A. AASLD guidelines for the treatment of hepatocellular carcinoma. *Hepatology* **67**, 358–380 (2018).

[6] Forner, A., Reig, M., Bruix, J. α-Fetoprotein for hepatocellular carcinoma diagnosis: the demise of a brilliant star. *Gastroenterology* **137**, 26–29 (2009).

[7] Wang, J. Electrochemical biosensors: towards point-of-care cancer diagnostics. *Biosens Bioelectron* **21**, 1887–1892 (2006).

[8] Kim, J., Jeong, J., Ko, S.H. Electrochemical biosensors for point-of-care testing. *Bio-Des Manuf* **7**, 548–565 (2024).

[9] Koyappayil, A., Yagati, A.K., Lee, M.-H. Recent trends in metal nanoparticles decorated 2D materials for electrochemical biomarker detection. *Biosensors* **13**, 91 (2023).

[10] Zhu, Y., Murali, S., Cai, W., Li, X., Suk, J.W., Potts, J.R., Ruoff, R.S. Graphene and graphene oxide: synthesis, properties, and applications. *Adv Mater* **22**, 3906–3924 (2010).

[11] Love, J.C., Estroff, L.A., Kriebel, J.K., Nuzzo, R.G., Whitesides, G.M. Self-assembled monolayers of thiolates on metals as a form of nanotechnology. *Chem Rev* **105**, 1103–1169 (2005).

[12] Kumarasamy, J., Camarada, M.B., Venkatraman, D., Ju, H., Dey, R.S., Wen, Y. One-step coelectrodeposition-assisted layer-by-layer assembly of gold nanoparticles and reduced graphene oxide and its self-healing three-dimensional nanohybrid for an ultrasensitive DNA sensor. *Nanoscale* **10**, 1196–1206 (2018).

[13] Benvidi, A., Dehghani-Firouzabadi, A., Mazloum-Ardakani, M., Mirjalili, B.-B.F., Zare, R. Electrochemical deposition of gold nanoparticles on reduced graphene oxide modified glassy carbon electrode for simultaneous determination of levodopa, uric acid and folic acid. *J Electroanal Chem* **736**, 22–29 (2015).

[14] Fernandez, R.E., Sanghavi, B.J., Farmehini, V., Chavez, J.L., Hagen, J.A., Kelley-Loughnane, N., Chou, C.-F., Swami, N.S. Aptamer-functionalized graphene-gold nanocomposites for label-free detection of dielectrophoretic-enriched neuropeptide Y. *Electrochem Commun* **72**, 144-147 (2016).

[15] Zheng, J., Feng, R., He, C., Li, X. Graphene-gold nanoparticle-modified electrochemical sensor for detection of kanamycin based on target-induced aptamer displacement. *Chem Res Chin Univ* **34**, 952-958 (2018).

[16] Wang, X., Han, Q., Yu, N., Li, J., Yang, L., Yang, R., Wang, C. Aptamer-conjugated graphene oxide-gold nanocomposites for targeted chemo-photothermal therapy of cancer cells. *J Mater Chem B* **3**, 4036-4042 (2015).

[17] Zhao, J., Chang, W., Liu, L., Xing, X., Zhang, C., Meng, H., Gopinath, S.C.B., Lakshmipriya, T., Chen, Y., Liu, Y. Graphene oxide-gold nanoparticle-aptamer complexed probe for detecting amyloid beta oligomer by ELISA-based immunoassay. *J Immunol Methods* **489**, 112942 (2021).

[18] So, Y.-H., Chang, H.-T., Chiu, W.-J., Huang, C.-C. Graphene oxide modified with aptamer-conjugated gold nanoparticles and heparin: a potent targeted anticoagulant. *Biomater Sci* **2**, 1332-1337 (2014).

[19] Deng, N., Jiang, B., Chen, Y., Liang, Z., Zhang, L., Liang, Y., Yang, K., Zhang, Y. Aptamer-conjugated gold functionalized graphene oxide nanocomposites for human alpha-thrombin specific recognition. *J Chromatogr A* **1427**, 16-21 (2016).

[20] Tah, A., Olmos Cordero, J.M., Weng, X., Neethirajan, S. Aptamer-based biosensor for food allergen determination using graphene oxide/gold nanocomposite on a paper-assisted analytical device. *bioRxiv*, 343368 (2018).

[21] Zhang, S., Chen, X., Hu, S., Cai, K., Peng, C., Luo, L., Gu, Y., Mei, Y. Electrochemical immunosensor based on PtNPs/MoS_2@rGO composite for the detection of alpha-fetoprotein in human serum. *Mikrochim Acta* **191**, 662 (2024).

[22] Kim, S.E., Sureshkumar, S., Kim, H.Y., Muthurasu, A., Yoon, J.C. Electrochemical sensitive detection of alpha-fetoprotein using HRP-gold nanostructures on Fe-Co MOF-derived nanocomposites. *ACS Appl Bio Mater* **8**, 10472-10482 (2025).

10.57647/jnsc.2026.1604.19

[23] Zhao, C.-L., Wang, H., Wang, X., Zhu, Y., Cai, B. Controllable methylene blue release/enrichment system for ultrasensitive electrochemical detection of alpha-fetoprotein. *Anal Chem* **97**, 24449-24457 (2025).

[24] Jian, H., Li, J., Zhao, S., Luo, Y., Wang, J., Liu, Z., Li, Y., Jiang, C. Self-powered cathode PEC sensor based on plasmonic excitation and PIRET signal amplification. *Microchem J* **224**, 117750 (2026).

[25] Zhang, Z., Wang, B., Wu, P., Jarnda, K.V., Tian, Y., Kai, T., Chen, C., Ding, P. Advances in optical and electrochemical aptasensors for tumor biomarker alpha-fetoprotein. *Mikrochim Acta* **193**, 107 (2026).

[26] Cao, Y., Xia, J., Li, L., Zeng, Y., Zhao, J., Li, G. Electrochemical biosensors for cancer diagnosis: multitarget analysis to present molecular characteristics of tumor heterogeneity. *JACS Au* **4**, 4655–4672 (2024).

[27] Gao, Y.-S., Zhu, X.-F., Yang, T.-T., Xu, J.-K., Lu, L.-M., Zhang, K.-X. Sensitive electrochemical determination of α-fetoprotein using a glassy carbon electrode modified with in situ grown gold nanoparticles, graphene oxide and MWCNTs acting as signal amplifiers. *Microchim Acta* **182**, 2027–2035 (2015).

[28] Liang, Y., Zhao, X., Wang, N., Wang, J., Chen, H., Bai, L., Wang, W. A label-free immunosensor based on PHEMA/graphene oxide nanocomposite for simultaneous electrochemical determination of alpha fetoprotein. *RSC Adv* **9**, 17187–17193 (2019).

[29] Piro, B., Reisberg, S. Recent advances in electrochemical immunosensors. *Sensors* **17**, 794 (2017).

[30] Radi, A.-E., Abd-Ellatief, M.R. Electrochemical aptasensors: current status and future perspectives. *Diagnostics* **11**, 104 (2021).

[31] Tuerk, C., Gold, L. Systematic evolution of ligands by exponential enrichment: RNA ligands to bacteriophage T4 DNA polymerase. *Science* **249**, 505–510 (1990).

[32] Stoltenburg, R., Reinemann, C., Strehlitz, B. SELEX—A (r)evolutionary method to generate high-affinity nucleic acid ligands. *Biomol Eng* **24**, 381–403 (2007).

[33] Dong, L., Tan, Q., Ye, W., Liu, D., Chen, H., Hu, H., Wen, D., Liu, Y., Cao, Y., Kang, J., Fan, J., Guo, W., Wu, W. Screening and identifying a novel ssDNA aptamer against alpha-fetoprotein using CE-SELEX. *Sci Rep* **5**, 15552 (2015).

[34] Song, K.-M., Lee, S., Ban, C. Aptamers and their biological applications. *Sensors* **12**, 612–631 (2012).

[35] Zhao, G., Liu, G. Electrochemical deposition of gold nanoparticles on reduced graphene oxide by fast scan cyclic voltammetry for the sensitive determination of As(III). *Nanomaterials* **9**, 41 (2019).

[36] Oberhaus, F.V., Frense, D., Beckmann, D. Immobilization techniques for aptamers on gold electrodes for the electrochemical detection of proteins: a review. *Biosensors* **10**, 45 (2020).

[37] Heiat, M., Negahdary, M. Sensitive diagnosis of alpha-fetoprotein by a label-free nanoaptasensor designed by modified Au electrode with spindle-shaped gold nanostructure. *Microchem J* **148**, 456–466 (2019).

[38] Zhu, C., Yang, G., Li, H., Du, D., Lin, Y. Electrochemical sensors and biosensors based on nanomaterials and nanostructures. *Anal Chem* **87**, 230–249 (2015).

[39] Wachholz Junior, D., Deroco, P.B., Hryniewicz, B.M., Kubota, L.T. Strategies for electrochemical point-of-care biosensors. *Annu Rev Anal Chem* **18**, 307–333 (2025).

[40] Yang, X., Yang, Z., Tang, F., Xu, J., Zhang, M., Choi, M.M.F. Structural and optical properties of penicillamine-protected gold nanocluster fractions separated by sequential size-selective fractionation. *Beilstein J Nanotechnol* **10**, 955–966 (2019).

[41] Burton, A.W., Ong, K., Rea, T., Chan, I.Y. On the estimation of average crystallite size of zeolites from the Scherrer equation: a critical evaluation of its application to zeolites with one-dimensional pore systems. *Microporous Mesoporous Mater* **117**, 75–90 (2009).

[42] Whetten, R.L., Khoury, J.T., Alvarez, M.M., Murthy, S., Vezmar, I., Wang, Z., Stephens, P.W., Cleveland, C.L., Luedtke, W., Landman, U. Nanocrystal gold molecules. *Adv Mater* **8**, 428–433 (1996).

[43] Adeel, M., Asif, K., Alshabouna, F., Canzonieri, V., Rahman, Md.M., Ansari, S.A., Güder, F., Rizzolio, F., Daniele, S. Label-free electrochemical aptasensor for the detection of SARS-CoV-2 spike protein based on carbon cloth sputtered gold nanoparticles. *Biosens Bioelectron X* **12**, 100256 (2022).

[44] García-Morales, N.G., García-Cerda, L.A., Puente-Urbina, B.A., Blanco-Jerez, L.M., Antaño-López, R., Castañeda-Zaldivar, F. Electrochemical glucose oxidation using glassy carbon electrodes modified with Au–Ag nanoparticles: influence of Ag content. *J Nanomater* **2015**, 295314 (2015).

[45] Behera, M. An intensive study on the optical, rheological, and electrokinetic properties of polyvinyl alcohol-capped nanogold. *Int Nano Lett* **5**, 161–169 (2015).

[46] Vestergaard, M., Kerman, K., Tamiya, E. An overview of label-free electrochemical protein sensors. *Sensors* **7**, 3442–3458 (2007).

[47] Formisano, N., Jolly, P., Bhalla, N., Cromhout, M., Flanagan, S.P., Fogel, R., Limson, J.L., Estrela, P. Optimisation of an electrochemical impedance spectroscopy aptasensor by exploiting quartz crystal microbalance with dissipation signals. *Sens Actuators B Chem* **220**, 369–375 (2015).

[48] Li, G., Li, S., Wang, Z., Xue, Y., Dong, C., Zeng, J., Huang, Y., Liang, J., Zhou, Z. Label-free electrochemical aptasensor for detection of alpha-fetoprotein based on AFP-aptamer and thionin/reduced graphene oxide/gold nanoparticles. *Anal Biochem* **547**, 37–44 (2018).

[49] Iordache, S.-M., Eusebiu, I., Iordache, A., Stamatin, I., Zoita, N., Sobetkii, A., Grigorescu, C. Functionalized carbon nanotubes for chemical sensing: electrochemical detection of hydrogen isotopes. *Coatings* **11**, 968 (2021).

[50] Sari, A.K., Gaffar, S., Hartati, Y.W. A review on the development of aptamer immobilization techniques in aptamer-based electrochemical biosensors for viruses detection. *Anal Bioanal Electrochem* **14**, 127-143 (2022).

[51] Brug, G.J., van den Eeden, A.L.G., Sluyters-Rehbach, M., Sluyters, J.H. The analysis of electrode impedances complicated by the presence of a constant phase element. *J Electroanal Chem Interfacial Electrochem* **176**, 275–295 (1984).

[52] Chang, B.-Y., Park, S.-M. Electrochemical impedance spectroscopy. *Annu Rev Anal Chem* **3**, 207–229 (2010).

[53] Tribollet, B. Analysis of constant phase element. *ECS Meet Abstr* **MA2013-01**, 1043 (2013).

[54] Lazanas, A.C., Prodromidis, M.I. Electrochemical impedance spectroscopy—A tutorial. *ACS Meas Sci Au* **3**, 162–193 (2023).

[55] Khalil, O.E., Elkordy, M.M. EIS information: use and quality determinants. *Inf Resour Manag J* **18**, 68–93 (2005).

[56] Holm, S., Holm, T., Martinsen, Ø.G. Simple circuit equivalents for the constant phase element. *PLoS One* **16**, e0248786 (2021).

[57] Wang, J., Kan, C., Gao, M., Jin, B. Ultrasensitive electrochemical aptasensor for alpha-fetoprotein detection based on cadmium telluride/cadmium selenide/polyaniline-cosensitized structure. *Electroanalysis* **37**, e12037 (2025).

[58] Olorundare, F.O.G., Sipuka, D.S., Sebokolodi, T.I., Kodama, T., Arotiba, O.A., Nkosi, D. An electrochemical immunosensor for an alpha-fetoprotein cancer biomarker on a carbon black/palladium hybrid nanoparticles platform. *Anal Methods* **15**, 3577–3585 (2023).

[59] Chen, H., Huang, J., Zhang, R., Yan, F. Dual-mode electrochemiluminescence and electrochemical sensor for alpha-fetoprotein detection in human serum based on vertically ordered mesoporous silica films. *Front Chem* **10**, 1023998 (2022).

[60] Wu, Y., Wang, Y., Wang, X., Wang, C., Li, C., Wang, Z. Electrochemical sensing of α-fetoprotein based on molecularly imprinted polymerized ionic liquid film on a gold nanoparticle modified electrode surface. *Sensors* **19**, 3218 (2019).

[61] Tsai, W.-C., Lin, I.-C. Development of a piezoelectric immunosensor for the detection of alpha-fetoprotein. *Sens Actuators B Chem* **106**, 455–460 (2005).

[62] Xie, B., Wang, H., Mochiwa, Z.O., Zhou, D., Gao, L. Highly sensitive detection of alpha-fetoprotein using sandwich sensors. *RSC Adv* **14**, 34661–34667 (2024).

[63] Krishna, D.N.G., Philip, J. Review on surface-characterization applications of X-ray photoelectron spectroscopy (XPS): recent developments and challenges. *Appl Surf Sci Adv* **12**, 100332 (2022).

[64] Ayiania, M., Smith, M., Hensley, A.J.R., Scudiero, L., McEwen, J.-S., Garcia-Perez, M. Deconvoluting the XPS spectra for nitrogen-doped chars: an analysis from first principles. *Carbon* **162**, 528–544 (2020).

[65] Ptasińska, S., Stypczyńska, A., Nixon, T., Mason, N.J., Klyachko, D.V., Sanche, L. X-ray induced damage in DNA monitored by X-ray photoelectron spectroscopy. *J Chem Phys* **129**, 065102 (2008).

[66] Wang, H., Qiu, X., Wang, W., Jiang, L., Liu, H. Iron sulfide nanoparticles embedded into a nitrogen and sulfur co-doped carbon sphere as a highly active oxygen reduction electrocatalyst. *Front Chem* **7**, 855 (2019).

[67] Li, X., Diao, Z., Dong, J., Liu, X., Luo, X., Hou, C., Huo, D. A homogeneous electrochemical aptasensor based on Pd@rGO and targeted methylene blue enrichment for sensitive detection of dibutyl phthalate. *Biosens Bioelectron* **291**, 118009 (2026).